RESEARCH ARTICLE

Multi-Layer Welding Path Correction of Medium-Thick Plate Based on Vision System

YUNLI LEI[1], LEI ZHANG[2,3], HUOSHENG DENG[1], LIN CHEN[3], AND HAIHONG PAN[3]

[1]School of Mechanical Engineering, Guangxi Technological College of Machinery and Electricity, Nanning 530004, China
[2]School of Physics and Telecommunications Engineering, Yulin Normal University, Yulin 537000, China
[3]School of Mechanical Engineering, Guangxi University, Nanning 530004, China

Corresponding author: Haihong Pan (hustphh@163.com)

ABSTRACT The multi-layer and multi-pass welding (MLMPW) process plays an important roll in the field of medium-thick plate automatic welding. To solve the problem of the robot self-adapting to the deviation of the weld position and the groove size due to the influence of the workpiece positioning and the welding deformation in MLMPW, a novel method based on the laser vision system to correct the path deviation is presented in this paper. Firstly, an image processing algorithm with image defogging technology is developed to deal with the interference problem of laser reflection on the metal surface. Then, the MLMPW path planning is performed based on the feature points extracted from the image. Lastly, a multi-layer welding path correction (MLWC) method is introduced to enable the robot to automatically scan the actual weld profile information of the previous layer and correct the welding path position of the next layer. The experiments demonstrate that the proposed MLWC method can effectively reduce scan times and eliminate the influence of welding deformation, and improve the adaptability of industrial robots to MLMPW.

INDEX TERMS Multi-layer welding, medium-thick plate, weld path correction, image defogging.

I. INTRODUCTION

In recent years, the use of robots in industrial manufacturing has significantly increased. Among the different industrial robots, welding robot plays a crucial role in reducing the cost of manual welding and improving the stability of welding quality [1], [2]. However, the existing welding robots operate on a 'teach-and-playback' mechanism [3], [4], which limits their capability to adapt to the welding process, especially the medium-thick plate welding.

Nowadays, medium-thick plate, which refers to the steel plate with a thickness exceeding 4 mm, is widely used in the domains of railway transportation, heavy machinery and marine ships [5]. The weld joint of a medium-thick plate is usually too large to weld completely at once.

The associate editor coordinating the review of this manuscript and approving it for publication was Shun-Feng Su.

Thus, multi-layer and multi-pass welding (MLMPW) is frequently utilized for medium-thick plate welding. However, the MLMPW process [6] is complex and needs to consider various factors including workpiece groove preparation, weld path planning, weld seam formation and weld joint quality. Therefore, most welding operations for medium-thick plates are still dominated by manual welding. An effective automated system module for MLMPW can boost the adaptability of welding robots and reduce production costs. Such a module has important theoretical research significance and engineering application value. Hence, the innovation and improvement of robot MLMPW has attracted considerable attention from various fields and is a hot spot in the field of welding robot research.

With the rapid development of machine vision and image processing technology, many vision sensors including monocular vision sensors, stereo vision sensors, 3D

vision sensors and structured-light vision sensors have been applied in robot automatic welding. Structured-light vision is a method of using laser-assisted measurements and has been used widely to measure the groove geometric dimension and track the weld seam. It has the advantages of simple structure, compact size, stable performance, uniform laser line width, large information and high accuracy [7].

The intelligence of the welding robots is improved when MLMPW is combined with the structured-light vision sensor. The multi-layer and multi-pass path pre-planning with the groove geometric dimension obtained from the scanned images can enable the welding robot to calculate and obtain the locations of each weld pass without the need for manual teaching [8]. The MLMPW is a complex processing process that is affected by various factors, such as the thermal deformation of the workpiece during the welding operation [6], the shape error from weld beads overlapping [9] and the cooling time of the inter-layer temperature [10], [11]. In such situations, the MLMPW path needs to be corrected. This problem is solved in this paper.

In a recent study on MLMPW adaptive path planning, the authors briefly reviewed the related works from two aspects.

A. ROBOTIC MLMPW ADAPTIVE PATH PLANNING

Robotic MLMPW path planning aims to reduce the time and cost of manual teaching. The main objective of robotic MLMPW path planning is to obtain an accurate welding path. Reference [12] used the scanning monocular stereo vision to reconstruct the 3D weld bead and provided a solid foundation for multi-layer multi-pass planning. Reference [13] constructed a double-sided double arc welding (DSAW) system with a self-designed passive vision sensor. The DSAW system performed the multi-pass path planning using the extracted welding parameters and the geometry size. However, the above-mentioned methods are only pre-planned for MLMPW paths. To resolve the issue of pre-planning path deviation caused by the workpiece deformation during multi-passes welding. References [14] and [15] performed finite element computations to predict the variation in the workpiece. However, this method is computationally heavy and requires offline planning. Reference [16] developed an adaptive pass adjustment scheme to address the discrepancies between the simulated results and the actual welding deposition after finishing a few layers of welding. However, the scheme lacked accurate dimension measurement of the weld seams and weld grooves by the visual system. References [17] and [18] obtained the MLMPW positions based on structured light images. However, the automation of MLMPW path correction needs to be further improved. Reference [19] proposed a scheme for extracting feature points of the weld seam profile to implement automatic multi-pass route planning and guidance of the initial welding position in each layer during Metal Active Gas (MAG) arc welding. However, since the workpiece continuously thermally deforms during welding, the accuracy of the welding position will be affected.

In summary, an effective MLMPW adaptive path planning should meet the following points. First, a precise weld measurement must be obtained to plan the MLMPW path. Second, the robot thick plate welding should be combined with the welding process, considering the tempering and cooling time of overlapped welding seams. Third, the deviation generated in the process of MLMPW should be efficiently corrected.

B. STUDY ON THE IDENTIFICATION ACCURACY OF WELD FEATURE POINTS BASED ON STRUCTURE-LIGHT VISION SENSOR

MLMPW path planning is based on the accurate measurement of the weld seam. Several studies have been conducted for improving weld seams identification accuracy. After obtaining the structural-light weld seam images, [20], [21] extracted the weld feature points through image processing. Reference [22] introduced deep learning to improve weld recognition accuracy. Reference [23] proposed a method of density-based clustering point cloud segmentation to acquire the weld seam position information. However, the extraction of laser stripe feature points would be affected by various interferences directly during image acquisition. Before welding, a reflection is produced by the laser stripes on the metal workpiece, which interferes with the extraction of the stripe centerline and affects the accuracy rate of weld seam recognition. In this paper, the image acquisition of line structure light is not implemented in the welding process. Thus, this paper only focuses on the filtering of laser metal reflection. To address this problem, some studies have adopted the hardware optimization method combining polarization camera and line structured light to locate weld [24]. However, this approach increased the hardware costs. Some studies have directly employed image processing methods to reduce interference. These image processing methods include image binarization [20] and a centre-line extraction algorithm based on skeleton extraction and RANSAC [24]. Nevertheless, the above image processing methods still need to perform further filtering in serious reflection interference situations. This paper proposes a novel method to filter the reflection. The proposed method can be combined with other image processing methods to further reduce the impact of interference on weld feature extraction.

Overall, a novel method based on the structured-light vision system is proposed to correct the path deviation and improve the intelligent level of welding robot in medium-thick plate welding operations. Firstly, since the scanned images have interference from the laser reflection on the metal surface, an image-defogging technology is developed for reducing the reflection. Secondly, the MLMPW path planning is constructed based on the feature points extraction from image processing. Finally, a multi-layer welding path correction (MLWC) method is introduced that enables the robot to automatically scan the actual weld profile information of the previous layer and correct the welding path position of the next layer.

The main contributions of this work are listed as follows.

- An image processing algorithm with image defogging technology is developed to solve the interference problem of laser reflection on the metal surface. The proposed algorithm can accurately collect the feature points of the groove and weld seams.
- A multi-layer welding path position correction method is proposed based on inter-layer scanning to reduce the influence of the weld groove deformation and improve work efficiency and the adaptability of the industrial robot to multi-layer welding. This method corrects the welding path position of the next layer by scanning the weld actual profile data of the previous layer.

The rest of this paper is organized as follows: Section II describes image processing, weld path planning, and weld path position correction method. Section III presents experimental research on V-type welding with the MLWC method. Finally, the conclusion is summarized in Section IV.

II. METHOD

The construction of a laser vision system is shown in Fig. 1, which consists of a CCD camera, line-structured light emitter and shell. Based on the principles of triangulation and pinhole imaging, the line-structured light emitter projects the laser onto the surface of the thick plate workpiece, forming a laser stripe with geometry. The CCD camera captures the images of welds with laser stripes and transmits them to the computer for image processing. This laser vision system is applied to obtain the information of weld features.
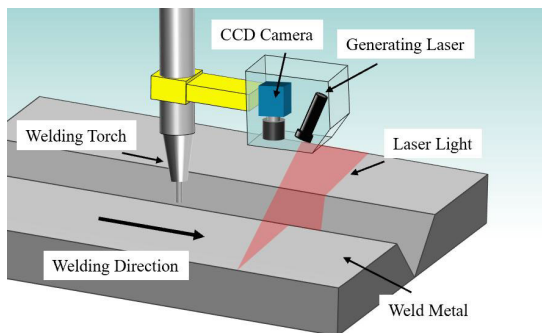

FIGURE 1. The line-structured light vision system.

A. THE PROCESS OF EXTRACTING FEATURE POINTS FROM AN IMAGE

One of the key research points in this paper is that the laser vision system is used to capture the weld feature points information in the robot base coordinate system. Then these extracted feature points are used to establish the three-dimensional model of different weld seams or grooves. Finally, the welding path is planned or corrected. In this paper, the feature points extraction process mainly includes Region of Interest (ROI) area extraction, reflection removal

processing with image-defogging, image filtering and binarization, area filtering, and center line extraction.

1) ROI AREA EXTRACTION

The YOLO [25], [26] was used to recognize and position the object in ROI area extraction. The YOLO has a fast running speed and is suitable for real-time systems.

In the ROI area prediction, YOLOv4 was used to directly predict the relative positions of the center point of the bounding box. YOLOv4 can detect the fusion features of multiple scales independently, and output three feature maps: y1, y2 and y3. The three feature map dimensions were set as 19×19, 38×38 and 76×76. To improve the prediction accuracy in different feature layers, the features of the low and high levels are integrated. The model was trained with 1421 images of laser stripe including 356 original images in different robot poses and 1056 images after data augmentation. The extraction of the ROI area is related to the image pixels and can be applied in the laser strip identification of weld seams or grooves regardless of the shape of the laser stripes. The model was constructed and trained with the pretrained model of YOLOv4 and the data was annotated with the samples.

ROI area extraction includes four steps:

(1) Collect weld laser stripe images of different robot poses as the input data, manual marking the ROI area as the output data, and then train the YOLOv4 model offline.
(2) Capture the original laser stripe images online.
(3) Output the weld identification results and confidence scores by the YOLOv4 model. The output bounding box includes confidence, center coordinates, width and height. The coordinate information of the upper left and lower right corners of the bounding box can be obtained according to the output parameters.
(4) Extract the ROI region from the image with the coordinate information obtained in Step 3 (Fig. 2).

The training environment consisted of windows10 64 bit, i9 9000k CPU, NVIDIA GeForce RTX 2060 graphics card and 16 GB memory (learning rate was set to 0.01 and the number of training times was 10000 times).

The ROI image is shown in Fig. 2, and its size is 720×540 pixels, which is only 30.45% of the original image. The trained YOLOv4 model was tested with five random groups each containing 20 images, and the ROI region images were automatically trimmed. The overall duration was less than 15ms.

2) IMAGE-DEFOGGING FOR REFLECTION REMOVAL

When the weld laser stripe images were captured, significant interference data arose due to the mirror reflection of the metal surface and bright reflective and diffuse reflection on the workpiece surface. Hence, the images could not be used directly. Since the quality of the weld laser stripe image directly affects the accuracy of the weld path planning, it is
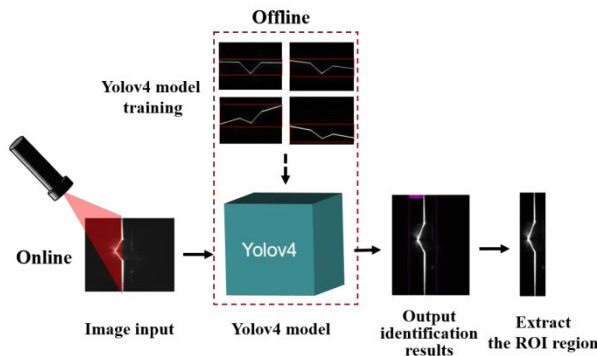
FIGURE 2. ROI area extraction.

essential to process the images and remove the interference data.

Here, an image-defogging algorithm is introduced to remove the reflection. The image-defogging algorithm is an image analysis and processing method that is designed to meet the requirements of specific scenes by highlighting the details of the image and enhancing the image quality. The image-defogging algorithm can solve blurred details, low contrast and the loss of important image information. The reflective phenomenon on the image of the weld laser stripe is similar to the fog (Fig. 3). Therefore, the image-defogging algorithm is used to remove the reflective phenomenon, and extract the clean and complete laser strips. This processing is done after the ROI images are extracted.

| (a)fog pictures | (b)Laser weld reflective picture |

FIGURE 3. The comparison of laser strip reflective image and fog image.

A physical model is usually used to describe the impact of severe weather conditions such as haze on the image, which includes two parts: an attenuation model and an ambient light model. The physical model is expressed as:

$$H(x) = F(x)e^{-rd(x)} + A(1 - e^{-rd(x)}) \qquad (1)$$

where x represents the spatial coordinates of the image pixel, H is the observed foggy image, F is the fog-free image to be recovered, r represents the atmospheric scattering coefficient, d represents the scene depth and A is the global atmospheric light, usually assumed global constant and is independent of the spatial coordinates (x). $F(x)e^{-rd(x)}$ is called a direct decline and shows that the reflected light on the surface of the scene is reduced by scattering when propagating in the medium. Let $L(x) = A(1 - e^{-rd(x)})$, namely ambient light,

which causes the image color and brightness offset. Then, Eq (1) is rewritten as Eq (2).

$$H(x) = F(x)(1 - \frac{L(x)}{A}) + L(x) \qquad (2)$$

The ambient light $L(x)$ and the global atmospheric light A are estimated from the image $H(x)$ to restore a clear fog-free image $F(x)$. Liu et al. [27] estimated the ambient and global atmospheric lights using mean filtering. In the process of removing the reflection, the laser vision system captured the weld laser stripe images in the form of single-channel gray maps. Hence, the gray value of each pixel is directly assigned instead of obtaining the minimum value corresponding to 3 channels for each pixel by traversal. The original formula $M(x) = \min(H^c(x))$ is changed into $M(x) = H(x)$. In the estimated transmission rate $t(x)$, estimated transmissivity after mean filtering can reflect the general trend of $t(x)$. However, there is a deviation from the true value. Therefore, the result of the mean filter compensates for an offset value. Here, the proportional coefficient of the compensation $\delta(0 \leq \delta \leq 1)$ is calculated from the reference [27]. When the value of δ is smaller, the final image has more residual reflective noise, leading to an overall brighter appearance. Conversely, with a larger value of δ, the final image controls the reflection obviously, resulting in a darker overall appearance. The values of δ are altered for comparing the different removal effects of reflection in Fig. 4.

Since a larger δ value results in a darker image and better corresponding removal effects of reflection, $\delta = 0.9$ is chosen. Moreover, since the dark image will be binarized in the subsequent steps, the rest of interference can be ignored.

3) IMAGE FILTERING AND BINARIZATION
The image is affected by the external environment and noise interference. Thus, image filtering is used to remove the noise and retain the maximum information of weld laser stripes. The median filtering mode is selected for image noise reduction processing (Fig. 5a). The median filtering method is a nonlinear smoothing technique that replaces the gray value of each pixel with the median gray value of all neighboring pixels. This image filtering mode has the characteristics of eliminating isolated noise points and protecting the laser stripe edge from being blurred.

After median filtering, the grayscale of the weld image is converted by binarization. During the binarization process, pixel values exceeding the predetermined threshold are set to 255, while values below the threshold are set to 0. This operation converts the image into a binary form, displaying only two grayscale levels: black and white (Fig. 5b).

4) AREA FILTERING
The outline of the laser stripe is obtained in the binarization image, but some indelible interferences are contained in the images due to laser line reflection. This part of the interference region is generally small and mostly unconnected with the laser stripe. Each connected region's area is detected and
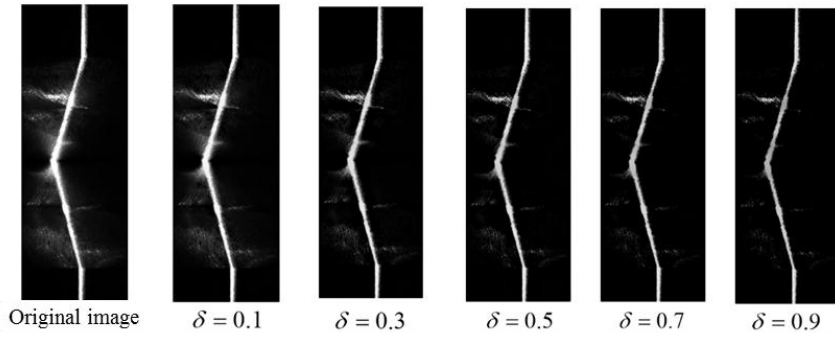
FIGURE 4. Different values of δ on reflective removal effect.
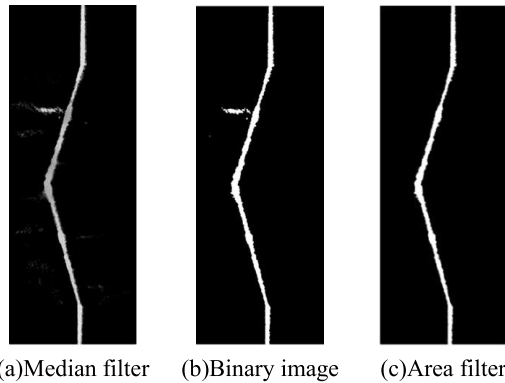

FIGURE 5. The process of removing interference from the images.

FIGURE 6. The principle of the row-by-row (column) search method.

the connected regions with an area less than the threshold (set value of 150) are removed as the interference points (Fig. 5c).

When the interference noises are on the laser stripes, the method of fitting function is adopted to accurately isolate and eliminate noises for extracting the feature points. Again, the fitting function method is applied in a weld 3D model establishing to effectively remove the feature points affected by noise.

5) CENTER LINE EXTRACTION

After binarization and area filtering, the image pixels are searched row-by-row (column) from left to right (from top to bottom). In each row (column) of the pixel's search, the pixel point with the first gray value of 255 is recorded as point A having pixel coordinates (x_0, y_0). The pixel point with the last gray value of 255 is recorded as point B with pixel coordinates (x_1, y_1) (Fig. 6).

In the current pixels search row (column), the laser stripe's center coordinates are extracted as $(\frac{x_0+x_1}{2}, \frac{y_0+y_1}{2})$. The center coordinates of the rows (columns) are iterated over to finally extract the laser stripe's center line in the whole image (Fig. 7).

6) WELD FEATURE POINT EXTRACTION

The weld groove information can make suitable welding process and welding path planning, which includes weld center feature point, reference point and weld width.

On the V-type butt weld workpiece (Fig. 8), the image's certain characteristic information is formed by the line structure light of the laser vision system. The geometric characteristics of the special point on the center line are significantly different from the others. The feature points are obtained from special points such as extreme points and end points. Then the appropriate welding process and welding path planning can be formulated according to these feature points.
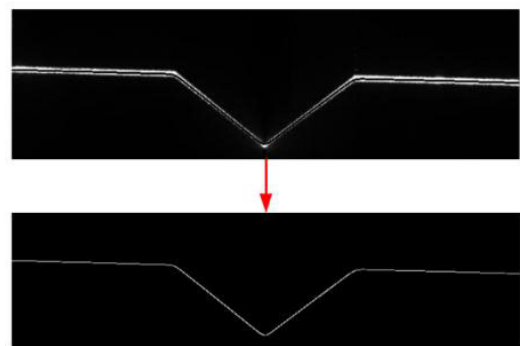

FIGURE 7. Laser stripe's center line extraction.

Assuming N and M are the start and end points on the center line of the laser stripe, respectively (Fig. 9). A certain amount of pixel points is selected from the beginning to the end on line NM. Here the amount is set as 70. Then the coordinates of the pixels are used to fit the line NM by least squares:
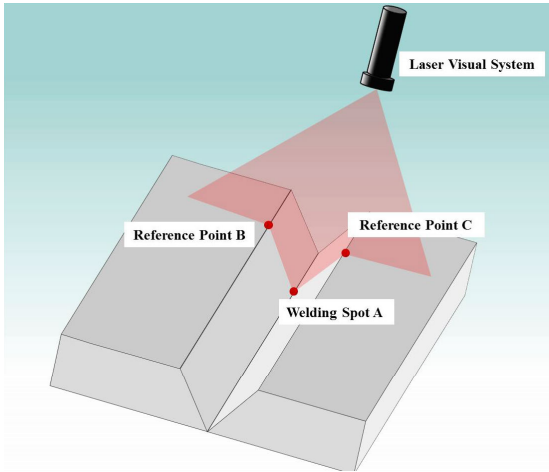
$$x + 0.03249y - 150.36971 = 0 \qquad (3)$$

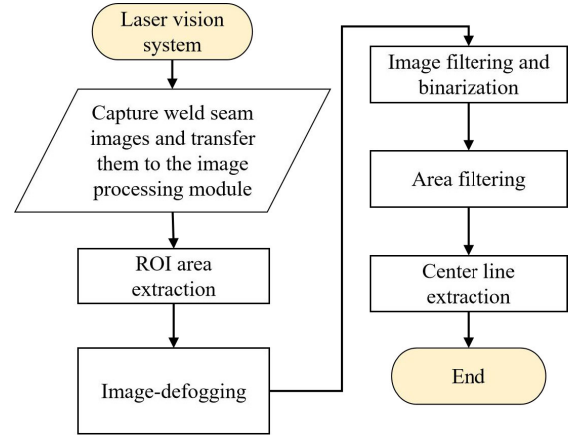**FIGURE 8.** The feature points of the butt V-shaped weld.

FIGURE 9. V-type groove feature point extraction.

FIGURE 10. The flowchart of image processing.

FIGURE 11. V-shaped weld cross section and coordinate system.

The distance between the pixels on the laser stripe center line and the fitted line NM is calculated and the laser stripe center line is divided into two parts: straight line NM and broken line BAC.

The adjacent pixel points B and C are found, they are the largest distance on the line NM. Then, point A of the largest distance is determined by iterating over the vertical distances from each pixel point on the broken line BAC to the straight-line NM.

The flowchart of image processing is shown in Fig. 10.

B. WELDING PATH PLANNING

After all the workpiece feature points of multiple images are obtained, a weld 3D model is constructed by establishing the feature point projection model and fitting the lines with the least squares method. Next, the trapezoidal and parallelogram weld path-filling strategies and the equal height-filling strategy are adopted to realize the planning of the V-type groove welding path. The coordinate system of the multi-layer multi-pass weld model is shown in Fig. 11.
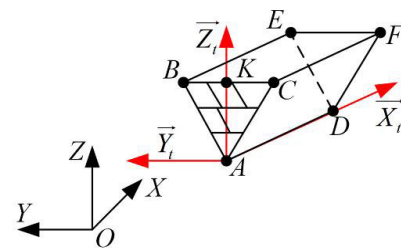
The first layer of bottom welding is simplified to a triangular weld path for the planning of welding torch position and posture. The arrangement of each weld pass follows the arithmetic progression. The weld path is planed with n weld passes ($n > 1$) in the n-th welding layer. A trapezoidal weld path is used as the last weld pass of each layer. The parallelogram weld path is applied for filling with remaining weld passes [16]. The primary goal of welding path planning is to achieve precise control over the profile size of the welds being formed. This control is accomplished by aligning the weld path sizes with the cross-sectional area of the weld seam.

C. MULTI-LAYER WELDING PATH POSITION CORRECTION
To eliminate the deformation effect after welding and the height change of each layer, the torch gun's start and end positions on the next layer are obtained by scanning and building the weld seam 3D information of the current weld. To improve the efficiency of the thicker workpiece welding, a strategy can be employed where every 2 or 3 weld layers can be scanned simultaneously, and the deviation of the 2 or 3 weld layers can be eliminated by correcting the next layer welding position.

1) THE RESCANNED WELD SEAM IMAGE FEATURE EXTRACTION
After each layer is welded, the weld images of V-type are roughly trapezoidal (Fig. 12). The feature points A1, A2, B

and C of the weld seam profile are acquired from the welding pass image feature information.

The feature points, the edge points of the weld groove (points B and C) and the width edge points of the welding path (points A1 and A2), are extracted from the weld image of each layer as shown in Fig. 13.
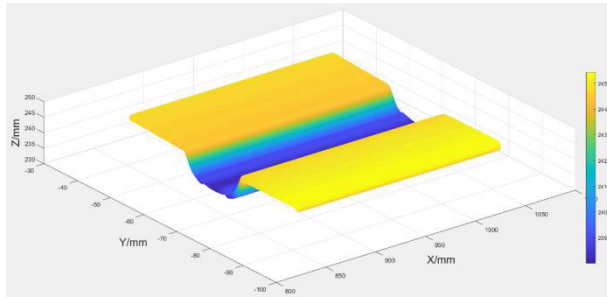

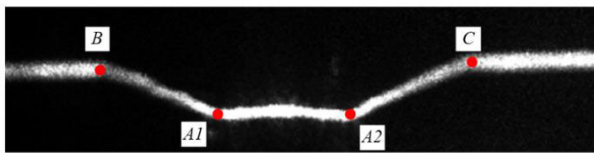**FIGURE 12.** The rescanned image 3D model of a V-type weld seam.

FIGURE 13. Weld image after rescanning.

The skeleton line (Fig. 14) is obtained after extracting the image ROI area, denoising and binarization (using the image processing method described in Section A).

FIGURE 14. The skeleton line of the weld image.

The skeleton line is divided into straight segment NM and fold line segment B-A1-A2-C. The pixel points B and C, the largest line gap, are obtained by comparing the distance difference between every two adjacent pixels on the line NM (Fig. 15).
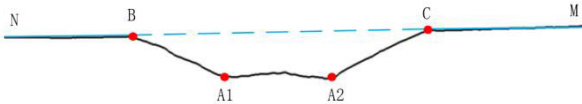

FIGURE 15. The skeleton line for the threshold segmentation.

The fold line segment B-A1-A2-C is divided into left and right, which are processed with Hough line detection and K-means clustering respectively. The contained straight lines are detected by the Hough transform. The K-means cluster
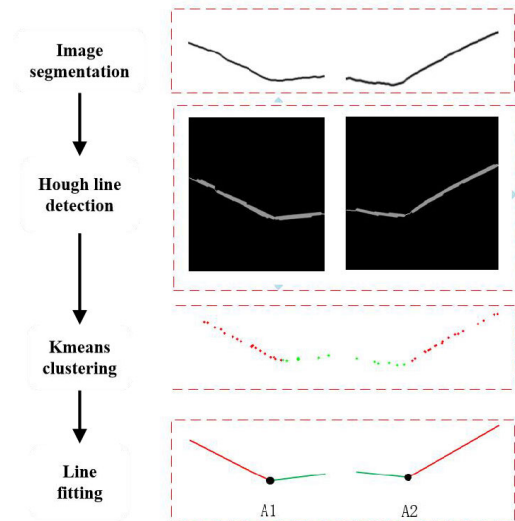

FIGURE 16. A straight-line fitting process based on K-means clustering.

category K is set as 2 and the K-means clustering dataset input is set as the line detection of straight slope k, intercept b, the start and end points. Two classes of cluster points are obtained, and then the lines of cluster points are fit using the least squares method. The intersection of the two lines is the weld feature points A1 and A2 (Fig. 16).

2) WELD PATH POSITION CORRECTION

Under the robot base coordinate system, the coordinates of the corresponding feature points are obtained by building 3D conversion and the projection, as follows: $A1_i = (x1_i, y1_i, z1_i)$, $A2_i = (x2_i, y2_i, z2_i)$, $B_i = (x3_i, y3_i, z3_i)$, $C_i = (x4_i, y4_i, z4_i)$. Weld path position corrections are mainly divided into two classes including left-right offset 'offset1' and the up-down offset 'offset2' and the combination of the two as shown in Fig. 17.

For the docked V-type multi-layer multi-pass weld model, the corresponding weld width of layer i is Wd_i and the starting point coordinate of the first pass of the layer is P_{i1}. The distance between the point $A1_i$ to the line B_iC_i is marked as t_i:

$$Wd_i' = \left| \overrightarrow{A1_iA2_i} \right| \tag{4}$$

$$Wd_{i+1}' = \frac{\left| \overrightarrow{B_iC_i} \right|}{t_i} \cdot h \tag{5}$$

where Wd_{i+1}' is the weld width of layer $i+1$ after welding layer $i-1$ and h is the height of each layer of the weld during pre-planning. The weld width of the i and $i+1$ layers are Wd_i' and Wd_{i+1}', respectively.

The positions of welding start and end points are replanned according to the equal height layer strategy and the filling strategy of n welding passes in the n-th welding layer. The equal area design method of inter-layer welding pass is used

to divide the width w_{ij} of each i-layer welding pass.

$$
\begin{cases}
w_{ij} = 0 & i = 1 \\
w_{ij} = \dfrac{Wd_i' + Wd_{i+1}'}{2i} & i \neq j \\
w_{ij} = Wd_i' - \dfrac{(i-1)\left(Wd_i' + Wd_{i+1}'\right)}{2i} & i = j
\end{cases}
\quad (6)
$$

Under the ideal model of a multi-layer multi-pass weld, the coordinates of the new weld point p_{ij} of the j weld pass in i layer are:

$$
p_{ij} = \overrightarrow{A} + (i-1) \cdot \frac{\overrightarrow{AB}}{n} + (j-1) \cdot w_{ij} \cdot \frac{\overrightarrow{BC}}{\left|\overrightarrow{BC}\right|} \quad j < i \quad (7)
$$

The coordinates of the start point p_{ij} of the last trapezoidal path of i weld layer are:

$$
p_{ij} = p_{ij-1} + \left[w_{ij-1} + \frac{w_{ij}}{2}\right] \cdot \frac{\overrightarrow{BC}}{\left|\overrightarrow{BC}\right|} \quad i = j \quad (8)
$$

Similarly, the weld point coordinates of each weld path in the i-layer are obtained. The welding path is planned with the straight-line interpolation method.
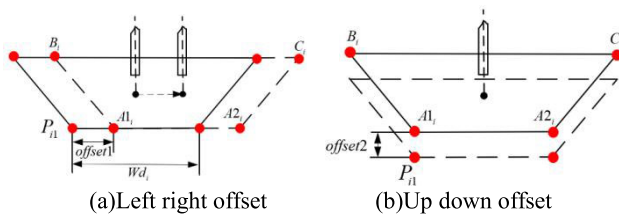

(a) Left right offset   (b) Up down offset

FIGURE 17. The welding model offset.

For V-type multi-layer single-pass weld path (Fig. 18), the corresponding midpoint coordinates M_i and N_i on lines $A1_iA2_i$ and B_iC_i are determined after completing the i-1 layer welding, respectively. The coordinates of the welding layer start point p_i and endpoint q_i are:

$$
p_i = \overrightarrow{A} + \overrightarrow{AM_i} + 0.5h \cdot \frac{\overrightarrow{M_iN_i}}{\left|\overrightarrow{M_iN_i}\right|} \quad (9)
$$

$$
q_i = \overrightarrow{A} + \overrightarrow{AD} + \overrightarrow{AM_i} + 0.5h \cdot \frac{\overrightarrow{M_iN_i}}{\left|\overrightarrow{M_iN_i}\right|} \quad (10)
$$

The weaving width W_{weave} of i layer is changed to:

$$
W_{weave} = 0.5h \frac{\left|\overrightarrow{B_iM_i}\right|}{\left|\overrightarrow{M_iN_i}\right|} \quad (11)
$$

Fig. 19 shows the system framework of the medium-thick plate welding with the MLWC method. Firstly, the workpiece groove is scanned by the line-structured light vision system before welding. Secondly, the scanned images are processed using the image-defogging algorithm to solve the problem of metal reflection. Thirdly, the welding path is pre-planned
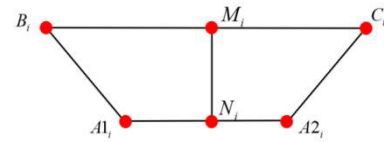

FIGURE 18. Multi-layer single-pass weld path calculation.

according to the extracted weld feature points information from the image. Then, the workpiece is welded by the welding robot under the welding parameters settings. After welding operation of each layer is completed, the weld inter-layer profile images are re-scanned by the robot. The welding path position of the next layer is corrected according to the pre-planning path and the new weld profile feature information, to reduce the effect of the weld groove deformation. The next layer is welded with the re-planed welding path position considering the cooling time required for the inter-layer temperature [10], [11]. Finally, the welding is finished when the last layer is completed.

The MLWC system was developed using C++ language based on Visual Studio 2017, OpenCV 3.4.1, and MFC. The communication between the system and the digital welding machine was based on the DeviceNet protocol. The independently developed welding robot control system can achieve collaborative control of robot motion and welding machine.

III. EXPERIMENTAL RESULTS
A. EXPERIMENT SETUP
The experimental platform consists of a welding robot and visual system: a six-axis robot body, digital welding machine, welding shield gas, wire feeder, welding torch, laser visual system and a flexible welding platform (Fig. 20).

To verify the MLWC method, a series of test experiments were designed, including the accuracy test, the V-type multi-layer single-pass welding experiment, and the V-type multi-layer multi-pass welding experiment.

B. THE LASER VISION SYSTEM ACCURACY TEST
To demonstrate the accuracy of the coordinates obtained by the laser vision system, the reference points were measured on the precision V-type groove, and the accuracy of the reference points was verified by theoretical calculation and actual position measurement (Table 1). The errors of coordinates X, Y and Z directions of the reference points were less than 0.8 mm, and the Root Mean Square Error (RMSE) is less than 0.674 mm, meeting the actual welding requirements.

C. V-TYPE MULTI-LAYER SINGLE-PASS WELDING EXPERIMENT
A V-type multi-layer single-pass welding (the material was Q235-A carbon structural steel, the thickness of the workpiece plate was 20 mm, and the weld groove width was 22 mm) was used as an experiment to verify the effectiveness of the weld pass position correction algorithm (Fig. 21). Each welded layer was rescanned, then the welding positions were
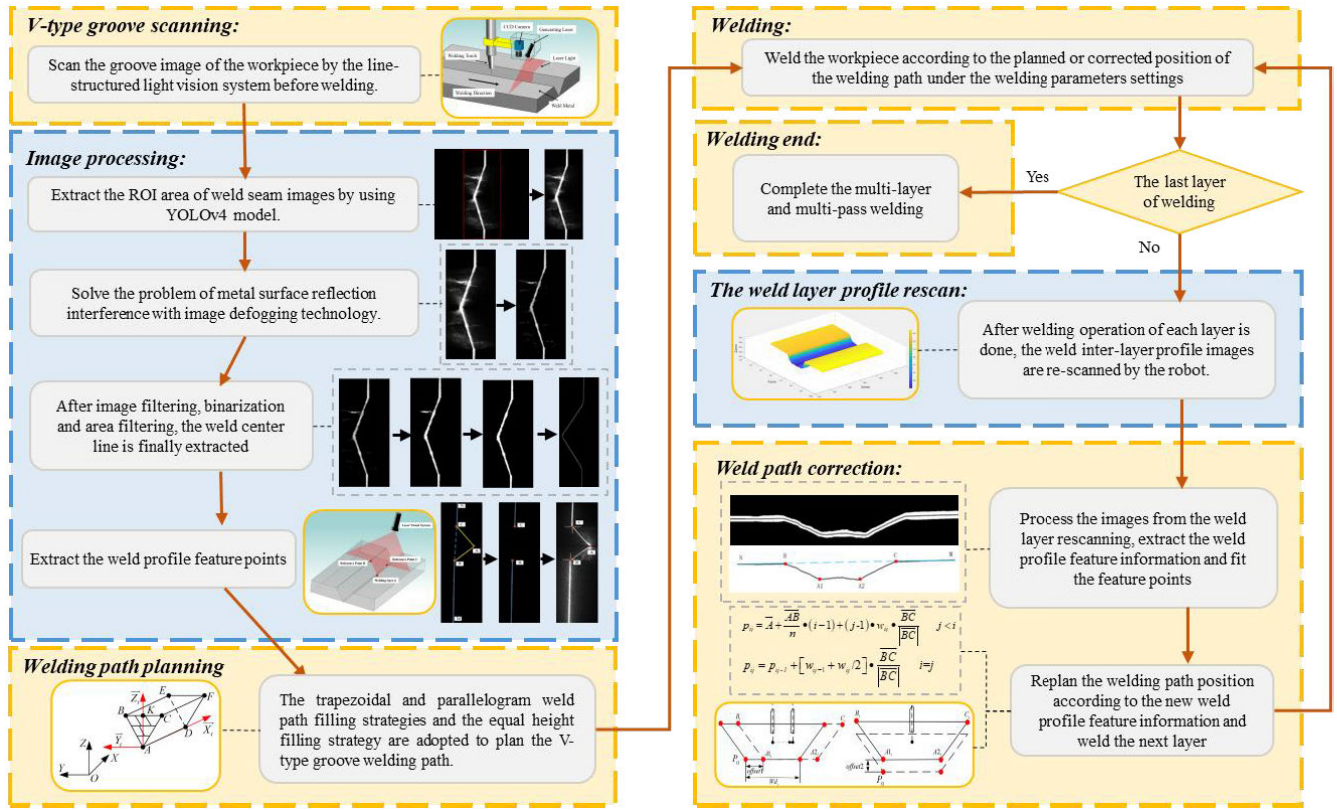
FIGURE 19. The system framework of the MLWC method.

TABLE 1. Accuracy test of the laser vision system.

| Welding features	Computing result(mm)	Manual test results(mm)	X direction error(mm)	Y direction error(mm)	Z direction error(mm)
Slope reference point B1	(1300.81,-79.872,337.285)	(1300.632,-79.762,338.019)	0.178	0.11	0.734
Slope reference point C1	(1300.99,-98.567,337.053)	(1300.591,-98.959,337.848)	0.399	0.392	0.795
Slope reference point B2	(1044.78,-52.976,338.614)	(1044.432,-52.187,337.843)	0.348	0.789	0.771
Slope reference point C2	(1044.19,-71.288,337.524)	(1044.452,-70.514,337.295)	0.262	0.774	0.229
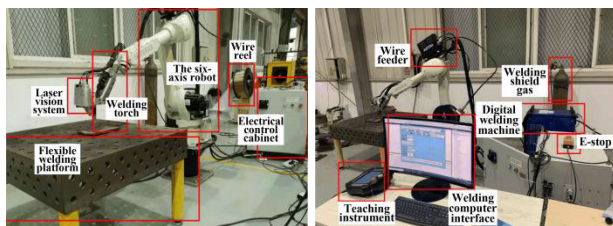
FIGURE 20. Welding robot experimental platform.

fine-adjusted and a new path for the V-type welding was planned. CO_2 was used as the protective gas. The gas flow was 18 L/min, and the welding wire diameter was 1.2 mm.

The number of welding layers was set as 4 layers. To achieve a satisfactory fusion between the welding wire and the side wall of the base material during the welding process, the triangle swing arc welding technique was applied to each layer. Specifically, the residence time on both sides of the inclined triangle swing arc was increased to 0.3 second. Table 2 shows the planning of the welding process for each layer of the weld.

To verify the correctness of the welding pass correction algorithm, the laser vision system was applied to continuously scan the welding layer profile information, and an approach similar to the 3D model was employed to construct the virtual welding seam profile of each layer. The test steps

(a) Before welding   (b) During welding   (c) Finish welding

FIGURE 21. Multi-layer single-pass welding of thick plate.

are as follows. (1) The start and end coordinates of the robot TCP for the first laser sensor scan were determined. Then each scan of the robot followed this path with a constant speed. (2) The weld images were captured and then the three-dimensional position information of the laser stripe in the robot base coordinates was calculated through image processing and the triangle projection theorem. (3) This series of images were combined to establish complete weld profile information, and the average height variation of the weld was calculated by taking 10 points on the weld profile. This method can visualize the acquired data and has the advantages of high accuracy without requiring physical contact compared with the traditional weld height measurement techniques. It is essential to ensure that the hand-eye calibration error remains below 0.5 mm for optimal results.

TABLE 2. Multi-layer single-pass welding process planning.

Welding layers	Welding pass	Current (A)	Voltage (V)	Speed (mm/s)	weaving width (mm)
1	1	190	23.5	8	0
2	2	180	23	15	4.1
3	3	260	27	15	6.9
4	4	255	26.5	10	9.6

D. V-TYPE MULTI-LAYER MULTI-PASS WELDING EXPERIMENT

To further validate the proposed MLWC method, a multi-layer multi-pass welding comparison experiment was performed. Two contrasting experiments were set up. Experiment A served as the control group. A docked V-type weld workpiece groove model was established with laser vision system scanning for pre-planning the welding path, and welding was performed directly along the pre-planned welding path. Based on experiment A, experiment B used the MLWC method to weld. The material conditions of the two experiments were consistent, the base material was Q235-A carbon structural steel, the protective gas was CO_2, the gas flow rate was 18 L/min, and the diameter of the welding

TABLE 3. Multi-layer multi-pass welding process planning.

Welding layers	Welding pass	Current (A)	Voltage (V)	Speed (mm/s)
1	1	150	21.5	8
2	2, 3	190	23.5	8
3	4, 5, 6	200	24	8
4	7, 8, 9, 10	210	24.5	8
5	11, 12, 13, 14, 15	210	24.5	8

wire was 1.2 mm. The thickness of the workpiece plate was 20 mm, the width of the weld groove was 22 mm, and the number of welding layers was set as 5 layers. The welding process plan of each layer of the workpiece is shown in Table 3.

E. RESULTS AND DISCUSSION
1) EFFECTIVENESS ANALYSIS OF THE MLWC METHOD

In the V-type multi-layer single-pass welding experiment, the MLWC method was utilized to adjust the welding path once each welding layer was completed. The offsets of the pre-planned and actual starting points(MLWC method) are shown in Fig. 22.

Fig. 23 illustrates that the workpiece's upper surface height (z-axis) gradually increased with the number of welding layers, starting from 245 mm at the beginning and reaching 247 mm after welding. Meanwhile, the weld gap width decreased from 22 mm to 20 mm after welding. The reason for this phenomenon is that the workpiece was unevenly and temporarily heated by the welding heat source during welding. In this process, the weld seam melting caused compressive plastic deformation from thermal expansion when the material temperature rose in the near-seam area, and the expansion process was constrained by the low-temperature material around it. While cooling, the materials undergoing compressive plastic deformation were confined by the surrounding cold materials, restricting their ability to contract freely. Simultaneously, the cooling shrinkage of the weld seam was constrained as the melting pool solidified, leading to tensile stress and deformation.

The average height of the first welding layer 3D profile (Fig. 23b) was about 6.5 mm, and the ME between actual weld seam and pre-planned weld path reached 1.5 mm. The welding layer was higher in the middle and lower on both sides, and the range reached 1 mm. The average height of the weld in the 3D profile of the second layer (Fig. 23c) was about 6 mm, while the MLWC method strictly controlled the ME within 1 mm. Due to the residence time being added on both sides of the swing arc in the second layer of welding, the height of the weld seam's edges became higher than the middle, which was contrary to the first layer. In the third layer 3D profile (Fig. 23d), the average height of the weld was about 4 mm, and the ME was still controlled within 1 mm. In the 3D profile of the fourth layer (Fig. 23e), the
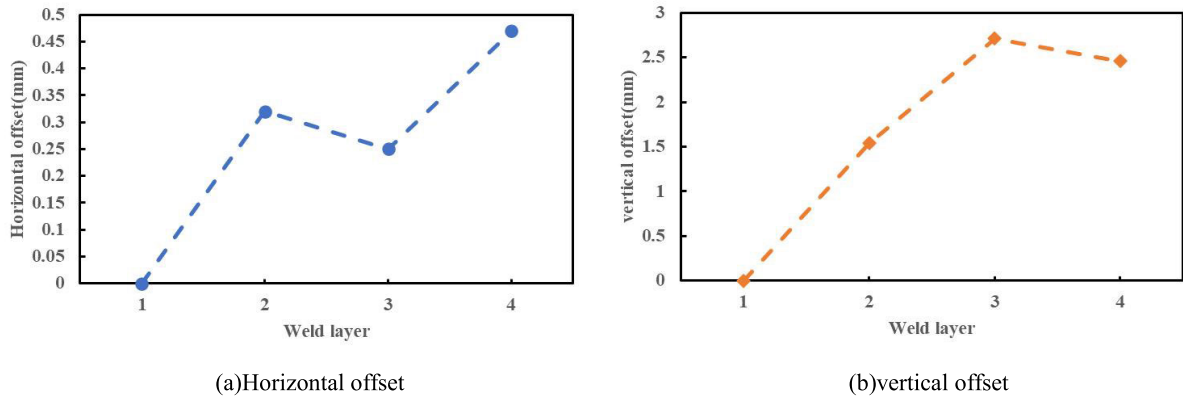
(a)Horizontal offset

(b)vertical offset

FIGURE 22. The offsets of the pre-planned starting points and actual starting points (MLWC method).

(a)3D profile of the groove before welding

(b)3D profile of the first layer of welding

(c)3D profile of the 2nd layer of welding

(d)3D profile of the 3th layer of welding

(e)3D profile of the 4th layer of welding
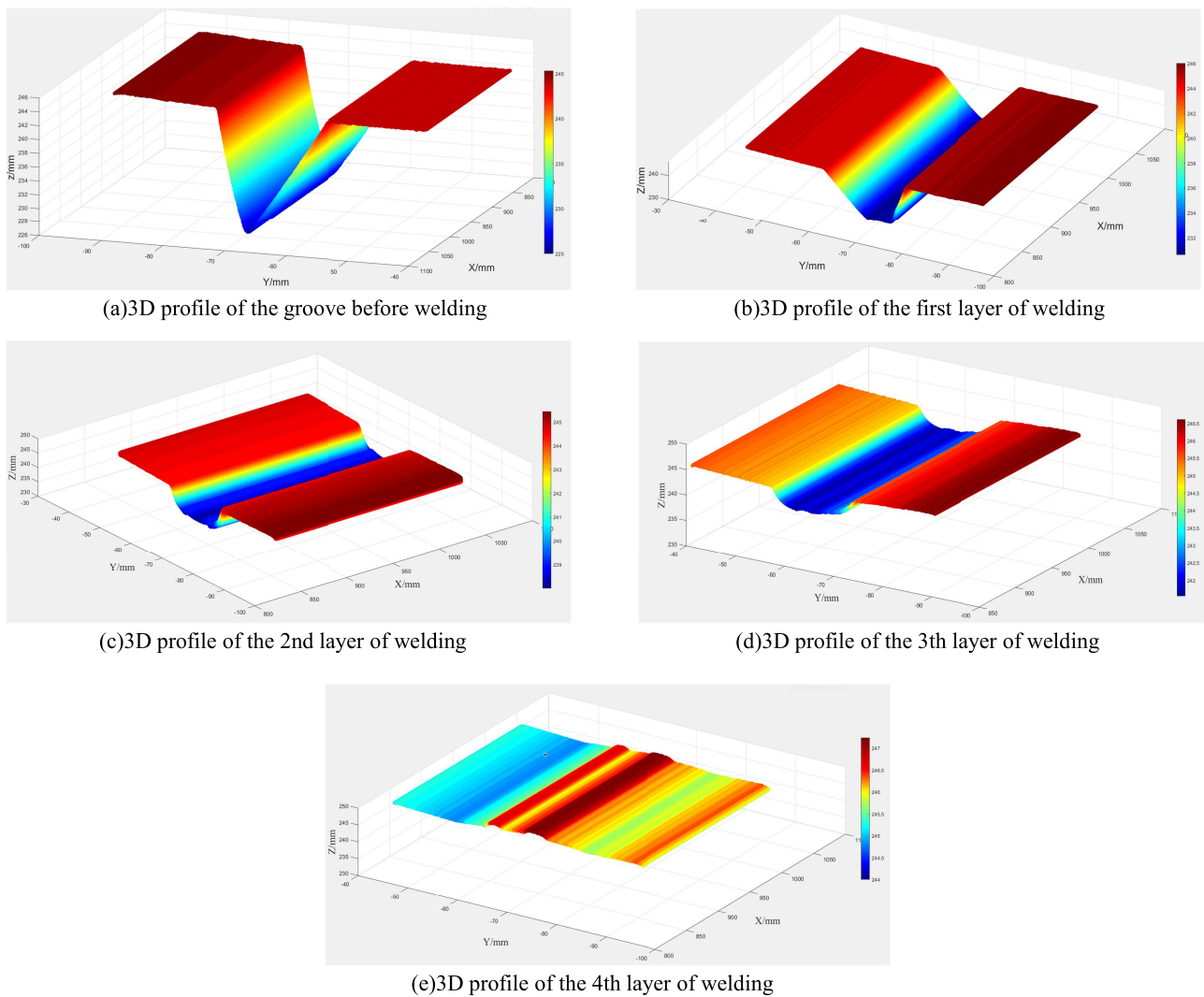
FIGURE 23. 3D profile of the multi-layer single-pass welding.

average height of the weld was about 4.5 mm, and the ME was 0.5 mm. Finally, the ME between the last weld layer and the workpiece surface was controlled within 2 mm.

Previously, He et al. [19] used the feature point extraction method to implement the positioning of the welding torch in each layer and multi-pass route planning during robotic

TABLE 4. The experimental results of one to four welding layers.

Welding layers	Experiment A (without MLWC method)	Experiment B (MLWC method)
1		
2		
3		
4		

MAG arc welding. However, this method simply locates the welding torch on the weld seam profile line, without effectively combining welding path planning. Hence, it would affect the overall geometric size of the weld joint. In this work, the MLWC method considers both the weld seam's cross-sectional area and the welding parameters of the next weld pass, This comprehensive consideration allows it to effectively control the geometric dimension deviation of the weld profile during multi-layer welding.

F. RESULTS AND ANALYSIS OF WELD SURFACE FORMED BY MLWC METHOD IN MULTI-LAYER MULTI-PASS WELDING

Experiment A (Table 4) performed direct welding according to the pre-planning welding path model. The visible angular deformation was produced during welding as the number of welding filling layers increased on the workpiece groove. Thus, the pre-planned welding path model was unable to adapt to the actual welding, which was most evident in the cover surface layer. The first welding pass of the fifth layer was more tended to the center line of the weld, and could not effectively fuse with the weld side wall. On the other hand, the fifth welding pass of the fifth layer was almost welded on the base metal plane, and the ME between the actual weld seam and the pre-planned weld path reached 3 mm. This deviation caused arc striking failure at the arcing point and resulted in excessively high weld height (Fig. 24).
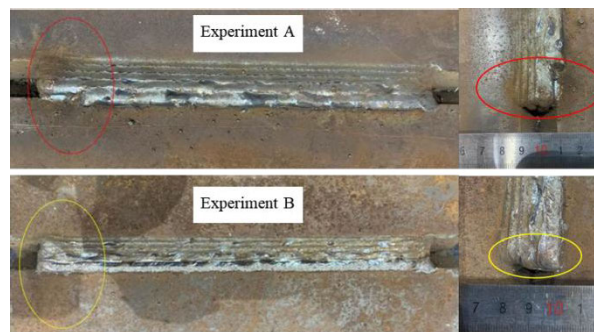

FIGURE 24. The fifth layer weld seam image.

The primary reason for the angular deformation was the uneven distribution of the material transverse contraction in the direction of the thick plate, which could result in transverse stress near the weld. The angular deformation was reflected in the workpiece, causing the two sides of the workpiece groove to bend upward with the weld as the center. As a result, both sides of the groove rose higher and the width of the weld became narrower.

In experiment B, the MLWC method was employed, which allowed the actual deformation to be adaptively adjusted by correcting the welding path. The weld joint was completely filled in the workpiece groove. The resulting welding surface matched the expected outcome precisely, meeting the desired effect as intended.

Yang et al. [28] used the method of scanning each weld pass and adjusting the next weld pass position, to correct the multi-layer weld path. However, it needed to scan every weld pass profile, which affected the efficiency. In the proposed MLWC method, the welding seam scanning was changed from weld pass to weld layer, and the number of scanning was reduced from 14 times to 4 times. This indicates the MLWC method can effectively improve the adaptability and efficiency of multi-layer and multi-pass automatic welding.

IV. CONCLUSION

An effective automated system module for Multi-Layer Multi-Pass Welding (MLMPW) can boost the adaptability of welding robots and reduce production costs. This paper proposes a method of multi-layer welding path correction, which involves adjusting the actual welding position to accommodate workpiece groove deformation during welding. Additionally, the paper resolves the issue of interference from metal surface reflection by employing the image-defogging technology processing algorithm. The experimental results demonstrate that the proposed MLWC method outperforms the traditional method without path correction in multi-layer automatic welding. The mean error (ME) between the last welding layer and the workpiece surface was controlled within 2 mm, and the number of scanning was reduced from 14 times to 4 times. The proposed method improves the adaptability and efficiency of industrial robots in multi-layer welding of the medium-thick plate.

The proposed multi-layer and multi-pass welding path planning and correction approach can be further enhanced by extending the MLWC method to be adaptable for various joint configurations, such as T-type joints, K-type joints and other joints. Further MLMPW experiments with weld beads overlapping model are essential to minimize the shape error. In addition to planning the welding path, incorporating the welding parameters such as welding speed, voltage and current, would significantly enhance the intelligence of the robotic MLPLW system.

REFERENCES

[1] B. Zhou, Y. Liu, Y. Xiao, R. Zhou, Y. Gan, and F. Fang, "Intelligent guidance programming of welding robot for 3D curved welding seam," *IEEE Access*, vol. 9, pp. 42345–42357, 2021, doi: 10.1109/ACCESS.2021.3065956.

[2] A. Rout, B. B. V. L. Deepak, and B. B. Biswal, "Advances in weld seam tracking techniques for robotic welding: A review," *Robot. Comput.-Integr. Manuf.*, vol. 56, pp. 12–37, Apr. 2019, doi: 10.1016/j.rcim.2018.08.003.

[3] B. Wang, S. J. Hu, L. Sun, and T. Freiheit, "Intelligent welding system technologies: State-of-the-art review and perspectives," *J. Manuf. Syst.*, vol. 56, pp. 373–391, Jul. 2020, doi: 10.1016/j.jmsy.2020.06.020.

[4] T. Haldankar, S. Kedia, R. Panchmatia, D. Parmar, and D. Sawant, "Review of implementation of vision systems in robotic welding," in *Proc. 5th Int. Conf. Intell. Comput. Control Syst. (ICICCS)*, May 2021, pp. 692–700, doi: 10.1109/ICICCS51141.2021.9432234.

[5] Y. Geng, M. Lai, X. Tian, X. Xu, Y. Jiang, and Y. Zhang, "A novel seam extraction and path planning method for robotic welding of medium-thickness plate structural parts based on 3D vision," *Robot. Comput.-Integr. Manuf.*, vol. 79, Feb. 2023, Art. no. 102433, doi: 10.1016/j.rcim.2022.102433.

[6] H. H. Zhao, H. C. Li, G. J. Zhang, Z. Q. Yin, and L. Wu, "Numerical simulation of temperature field and stress distributions in multi-pass single-layer weld-based rapid prototyping," *Rev. Adv. Mater. Sci.*, vol. 33, no. 5, pp. 402–409, Aug. 2013.

[7] S. Chen, J. Liu, B. Chen, and X. Suo, "Universal fillet weld joint recognition and positioning for robot welding using structured light," *Robot. Comput.-Integr. Manuf.*, vol. 74, Apr. 2022, Art. no. 102279, doi: 10.1016/j.rcim.2021.102279.

[8] D. Chang, D. Son, J. Lee, D. Lee, T.-W. Kim, K.-Y. Lee, and J. Kim, "A new seam-tracking algorithm through characteristic-point detection for a portable welding robot," *Robot. Comput.-Integr. Manuf.*, vol. 28, no. 1, pp. 1–13, Feb. 2012, doi: 10.1016/j.rcim.2011.06.001.

[9] D. Ding, Z. Pan, D. Cuiuri, and H. Li, "A multi-bead overlapping model for robotic wire and arc additive manufacturing (WAAM)," *Robot. Comput.-Integr. Manuf.*, vol. 31, pp. 101–110, Feb. 2015, doi: 10.1016/j.rcim.2014.08.008.

[10] M. A. Mousazadeh and R. Derakhshandeh-Haghighi, "Autogenous tungsten inert gas welding of 430 ferritic stainless steel: The effect of interpass temperature on microstructure evolution and mechanical properties," *J. Mater. Eng. Perform.*, vol. 29, no. 12, pp. 7807–7820, Dec. 2020, doi: 10.1007/s11665-020-05281-z.

[11] D. Yang, G. Wang, and G. Zhang, "Thermal analysis for single-pass multi-layer GMAW based additive manufacturing using infrared thermography," *J. Mater. Process. Technol.*, vol. 244, pp. 215–224, Jun. 2017, doi: 10.1016/j.jmatprotec.2017.01.024.

[12] Z. Hou, Y. Xu, R. Xiao, and S. Chen, "A weld bead profile extraction method based on scanning monocular stereo vision for multi-layer multi-pass welding on mid-thick plate," in *Transactions on Intelligent Welding Manufacturing*. Singapore: Springer, 2021, pp. 87–98.

[13] C. Yang, Z. Ye, Y. Chen, J. Zhong, and S. Chen, "Multi-pass path planning for thick plate by DSAW based on vision sensor," *Sensor Rev.*, vol. 34, no. 4, pp. 416–423, Aug. 2014, doi: 10.1108/sr-04-2013-649.

[14] M. Ericsson, D. Berglund, and P. Nylen, "Three dimensional simulation of robot path, heat transfer and residual stresses of a TIG-welded part with complex geometry," in *Proc. 6th Int. Conf. Trends Weld. Res.*, Phoenix, AZ, USA, 2003, pp. 973–978.

[15] F. Sikstrom, M. Ericsson, A. K. Christiansson, and K. Niklasson, "Tools for simulation based fixture design to reduce deformation in advanced fusion welding," in *Proc. 1st Int. Conf. Intell. Robot. Appl.* (Lecture Notes in Artificial Intelligence), 2008, pp. 398–407.

[16] H. C. Fang, S. K. Ong, and A. Y. C. Nee, "Adaptive pass planning and optimization for robotic welding of complex joints," *Adv. Manuf.*, vol. 5, no. 2, pp. 93–104, Jun. 2017, doi: 10.1007/s40436-017-0181-x.

[17] C. Zhang, H. Li, Z. Jin, and H. Gao, "Seam sensing of multi-layer and multi-pass welding based on grid structured laser," *Int. J. Adv. Manuf. Technol.*, vol. 91, nos. 1–4, pp. 1103–1110, Jul. 2017, doi: 10.1007/s00170-016-9733-7.

[18] J. Zeng, B. Chang, D. Du, L. Wang, S. Chang, G. Peng, and W. Wang, "A weld position recognition method based on directional and structured light information fusion in multi-layer/multi-pass welding," *Sensors*, vol. 18, no. 2, p. 129, Jan. 2018, doi: 10.3390/s18010129.

[19] Y. He, Y. Xu, Y. Chen, H. Chen, and S. Chen, "Weld seam profile detection and feature point extraction for multi-pass route planning based on visual attention model," *Robot. Comput.-Integr. Manuf.*, vol. 37, pp. 251–261, Feb. 2016, doi: 10.1016/j.rcim.2015.04.005.

[20] F. Guo, W. Zheng, G. Lian, and M. Yao, "A V-shaped weld seam measuring system for large workpieces based on image recognition," *Int. J. Adv. Manuf. Technol.*, vol. 124, nos. 1–2, pp. 229–243, Jan. 2023, doi: 10.1007/s00170-022-10507-6.

[21] W. P. Gu, Z. Y. Xiong, and W. Wan, "Autonomous seam acquisition and tracking system for multi-pass welding based on vision sensor," *Int. J. Adv. Manuf. Technol.*, vol. 69, nos. 1–4, pp. 451–460, Oct. 2013, doi: 10.1007/s00170-013-5034-6.

[22] Y. B. Zou, T. Chen, X. Z. Chen, and J. C. Li, "Robotic seam tracking system combining convolution filter and deep reinforcement learning," *Mech. Syst. Signal Process.*, vol. 165, Feb. 2022, Art no. 108372, doi: 10.1016/j.ymssp.2021.108372.

[23] B. Hong, A. T. Jia, Y. X. Hong, X. W. Li, J. P. Gao, and Y. Y. Qu, "Online extraction of pose information of 3D zigzag-line welding seams for welding seam tracking," *Sensors*, vol. 21, no. 2, p. 375, Jan. 2021, doi: 10.3390/s21020375.

[24] Z. Tan, B. Zhao, Y. Ji, X. Xu, Z. Kong, T. Liu, and M. Luo, "A welding seam positioning method based on polarization 3D reconstruction and linear structured light imaging," *Opt. Laser Technol.*, vol. 151, Jul. 2022, Art. no. 108046, doi: 10.1016/j.optlastec.2022.108046.

[25] C.-Y. Wang, A. Bochkovskiy, and H. M. Liao, "Scaled-YOLOv4: Scaling cross stage partial network," in *Proc. IEEE/CVF Conf. Comput. Vis. Pattern Recognit. (CVPR)*, Jun. 2021, pp. 13024–13033, doi: 10.1109/cvpr46437.2021.01283.

[26] J. Redmon, S. Divvala, R. Girshick, and A. Farhadi, "You only look once: Unified, real-time object detection," in *Proc. IEEE Conf. Comput. Vis. Pattern Recognit. (CVPR)*, Seattle, WA, USA, Jun. 2016, pp. 779–788, doi: 10.1109/cvpr.2016.91.

[27] Q. Liu, M. Chen, and D. Zhou, "Fast haze removal from a single image," in *Proc. 25th Chin. Control Decis. Conf. (CCDC)*, May 2013, pp. 3780–3785.

[28] C.-W. Yang, M.-C. Tsai, and C.-C. Chang, "Investigating the joint choice behavior of intercity transport mode and high-speed rail cabin with a strategy map," *J. Adv. Transp.*, vol. 49, no. 3, pp. 297–308, Apr. 2015, doi: 10.1002/atr.1264.

HUOSHENG DENG received the degree in mechanical design, manufacturing and automation from the Jiangsu University of Technology, Changzhou, China, in 2011. He is currently a Lecturer and a Senior Engineer with the Guangxi Technological College of Machinery and Electricity, Nanning, China. His current research interests include robot welding technology, robot systems, and intelligent manufacturing.

YUNLI LEI received the master's degree in computer engineering from Wuhan University, Wuhan, China, in 2011. He is currently pursuing the Ph.D. degree with Adamson University, Manila, Philippines. He is currently a Lecturer with the Department of Mechanical Engineering, Guangxi Technological College of Machinery and Electricity, Nanning, China. His current research interests include machine learning, intelligent algorithms, and welding engineering.

LIN CHEN received the Ph.D. degree from the Huazhong University of Science and Technology, Wuhan, China, in 2008. She is currently a Professor with the College of Mechanical Engineering, Guangxi University. Her current research interests include machine learning, numerical control, virtual reality, electromechanical detection and control technology used in rehabilitation robots industrial robot manipulators, and the battery management system in electric vehicles.

LEI ZHANG received the M.S. degree in mechanical engineering from the Guilin University of Electronic Technology, Guilin, China, in 2015. He is currently pursuing the Ph.D. degree with the School of Mechanical Engineering, Guangxi University, Nanning, China. He has been a Lecturer with the School of Physics and Telecommunication Engineering, Yulin Normal University, Yulin, China. His current research interests include machine learning, intelligence algorithms, thermal error compensation of machine tools, robotic control systems, and intelligent manufacturing.

HAIHONG PAN received the M.E. degree in mechatronic engineering from Guangxi University, Nanning, China, in 1991, and the Ph.D. degree in mechatronic engineering from the Huazhong University of Science and Technology, Wuhan, China, in 2007. He is currently a Professor with the College of Mechanical Engineering, Guangxi University. His current research interests include numerical control, virtual reality, electromechanical detection and control technology used in rehabilitation robots and industrial robot manipulators, deep learning, computer vision, and intelligent manufacturing.

● ● ●